Glory interference spectroscopy in Sr atom

K Ferentinou, S Danakas, C Bordas, S Cohen

Glory interference spectroscopy in Sr atom

To cite this article: K Ferentinou *et al* 2024 *J. Phys. B: At. Mol. Opt. Phys.* **57** 115002

OPEN ACCESS
IOP Publishing
Journal of Physics B: Atomic, Molecular and Optical Physics
J. Phys. B: At. Mol. Opt. Phys. **57** (2024) 115002 (12pp)
https://doi.org/10.1088/1361-6455/ad421e

Glory interference spectroscopy in Sr atom

K Ferentinou[1], S Danakas[1], C Bordas[2] and S Cohen[1,*]

[1] Atomic and Molecular Physics Laboratory, Physics Department, University of Ioannina, 45110 Ioannina, Greece
[2] Université de Lyon, CNRS, UMR5306, Institut Lumière Matière, 69622 Villeurbanne, France

E-mail: scohen@uoi.gr

Received 21 September 2023, revised 15 March 2024
Accepted for publication 23 April 2024
Published 8 May 2024

Abstract

Slow (meV) photoelectron imaging spectroscopy is employed in the experimental study of near-threshold photoionization of strontium atoms in the presence of an external static electric field. Specifically, the study is devoted to the glory effect, that is, the appearance of an intense peak at the center of the recorded photoelectron images, when dealing with $m = 0$ final ionized Stark states (m denoting the magnetic quantum number). This critical effect is formally identical to that encountered in classical scattering theory, where, for a nonzero value of the impact parameter, the zero-crossing of the deflection function leads to a divergent classical differential cross section. By recording the magnitude variation of this glory peak as a function of electron excitation energy, we observe that, besides the traces of classical origin, it also exhibits intense quantum interference and beating phenomena, above and below the zero-static-field ionization threshold. We study both, single- and two-photon ionization of Sr, thus enabling a comparison not only between the different excitation schemes, but also with an earlier work devoted to two-photon ionization of Mg atom by Kalaitzis *et al* (2020 *Phys. Rev.* A **102** 033101). Our recordings are analyzed within the framework of the Harmin–Fano frame transformation Stark effect theory that is applied to both the hydrogen atom and a non-hydrogenic one simulating Sr. We discuss the various aspects of the recorded and calculated glory interference and beating structures and their 'short time Fourier transforms' and classify them as either atom-specific or atom independent. In particular, we verify the 'universal' connection between the glory oscillations above the zero-field threshold and the differences between the origin-to-detector times of flight corresponding to pairs of classical electron trajectories that end up to the image center.

Keywords: Stark effect, photoionization, slow photoelectron imaging, glory effect

1. Introduction

Atomic photoionization studies in the vicinity of the ionization limit and in the presence of a static (DC) homogeneous electric field are of fundamental physical interest, and their investigation is enabled by the analysis of the properties of slow (meV) photoelectrons. Much of the phenomenology that is specific to slow photoelectrons is revealed by the examination of the differential ionization cross section. The latter is nowadays efficiently complemented by means of threshold photoelectron imaging spectroscopy, where the two-dimensional slow electron flux is projected (imaged) on a position sensitive detector (PSD), which brings an additional dimension to the experimental data. It is by now well understood that, apart from its possible applications in surface characterization [1], slow photoelectron imaging [2, 3] can provide information on the wavefunctions of continuum [4] and quasibound [5, 6] atomic Stark states, photoelectron momentum distributions transversely to

* Author to whom any correspondence should be addressed.

the DC field [3, 7–9] and the manipulation of Stark wavepackets by means of the laser polarization [10].

Of particular interest, and at the focus of the present work, is the information that slow photoelectron images may provide on electron dynamics [11, 12]. One possible way of achieving this goal is by considering the magnitude variation of the signal at the center of the images as a function of excitation energy. This central signal appears only in the images of final, excited Stark states with magnetic quantum number $m = 0$. It is particularly intense for meV electrons and in the presence of the DC field, since it originates from the critical effect of glory scattering. The term derives from classical particle scattering and characterizes the divergence of the classical differential cross section when the deflection function goes through zero for a nonzero impact parameter [13]. In the present case of the so-called Coulomb–Stark problem [2, 14, 15] the role of the deflection function is assumed by the impact radius ρ on the PSD, while the electron ejection angle β acts as the impact parameter (with $\beta = 0$ denoting ejection along the DC field direction and $\beta = \pi$ ejection towards the detector). Then, at any given excitation energy E, the glory signal is composed by the contributions of those source-to-detector classical trajectories that lead, under the action of the DC field, to the image center and correspond to the 'glory angles' β_k, $k = 0,1,2,\ldots$, such that $\rho(\beta_k) = 0$. For excitation energies above the zero-DC-field limit (i.e. for $E \geqslant 0$) the number of glory angles is infinite, though only a few trajectories substantially contribute. Thus, from a semiclassical point of view one would expect these multiple glory pathways to be responsible for the emergence of interference and beating effects that modulate the glory signal as E varies. These notions were recently found to be fully supported by hydrogenic quantum calculations and by an experiment devoted to two-photon threshold ionization of ground state Mg atoms [11]. As it turned out from that study, a 'short time Fourier transform' (STFT) [16] of either the calculated or the observed positive energy glory oscillations reveals their close connection with the time-delays between the arrival times on the PSD of the trajectory pairs corresponding to ejection angles $\beta = \beta_k$ and $\beta = \pi$. This is a formidable example of the correspondence principle in action, where such a piece of 'spectroscopic' information (which disappears and has no counterpart when the DC-field is turned-off) provides considerable insight into the underlying classical physics embedded in a quantum system. Even more, in contrast with most examples given in the literature so far [17], this correspondence implies here energy (quasi-)quantization in the continuum and refers to non-periodic classical motion.

The agreement between experiment and a hydrogenic (classical and quantum) theory on the $E \geqslant 0$ glory oscillations points towards the global character of these spectral structures, the details of which appear to be practically independent of any given target atom. As it was pointed out earlier, however, this expectation needs to be firmly established by performing measurements on other atomic systems, *a priori* heavier than magnesium, and under similar conditions.

Motivated by the above reasoning, the purpose of the present work is to extend glory interference spectroscopy measurements to Sr atom. The choice of this specific target atom is guided by our desire to retain a similarity with the Mg experiment, since Sr also belongs to the group of Alkaline Earth atoms with two valence electrons outside closed (sub)shells. Extending the similarities even further, the present study allows comparison of the results obtained by two-photon ionization. Due, however, to the relatively low first ionization threshold of strontium, its two-photon ionization is achieved with visible radiation of quite convenient wavelength. In fact, the frequency of the latter radiation can be easily doubled by an appropriate non-linear crystal and, therefore, a single-photon ionization study with ultraviolet (UV) radiation is also possible. Therefore, the present work allows, in principle, comparisons between different atoms with specific energy level Stark structures (at least for $E < 0$, i.e. below the zero-field limit) as well as between different photoionization schemes within the same atom. Furthermore, in order to facilitate the distinction between global and target-specific phenomena and observations, we employ the Harmin–Fano frame transformation Theory (FTT) [18–21] for calculating the Stark effect. The latter, can be applied for either hydrogenic or non-hydrogenic atoms. Finally, particularly for the $E \geqslant 0$ energy range, we also use the aforementioned classical time delay curves between the arrival times on the PSD, as discussed and computed in other works [11, 22].

The rest of the paper is organized as follows: In the next section we make a brief presentation of the quantum theoretical framework of near-threshold photoelectron imaging with emphasis on the glory signal and within the context of Harmin–Fano FTT. The third section is devoted to the brief description of the experimental setup and procedure. In the fourth section, the experimental glory spectra and their STFTs for the single- and two-photon ionization cases are presented, discussed, and compared with the relevant theoretical counterparts. Finally, in the last section we provide our conclusions and discuss possible directions of further work.

2. Theoretical description

The Schrödinger equation's solution for the near-threshold-excited hydrogen atom in the presence of a homogeneous static electric field $\mathbf{F} = F\mathbf{z}$ was abundantly described in earlier works [9–11]. Therefore its description here will be brief, emphasizing solely on the specific features concerning the glory effect and some necessary extensions regarding multielectron atoms. Starting with the hydrogenic, so-called, Coulomb–Stark problem, the corresponding potential energy is written in atomic units (a.u.) as $V(\mathbf{r}) = -Z/r + Fz$, with $r = [x^2 + y^2 + z^2]^{1/2}$ and Z the charge of the attractive center. The Schrödinger equation for $V(\mathbf{r})$ is separable in parabolic coordinates $\chi = [r + z]^{1/2} \geqslant 0$, $\upsilon = [r - z]^{1/2} \geqslant 0$ and $\varphi = \tan^{-1}(y/x)$ [23]. The wave function in these coordinates is written in the form $\psi(\mathbf{r}) = [2\pi\chi\upsilon]^{-1/2} X(\chi) Y(\upsilon) e^{im\varphi}$, where $m = 0, \pm 1, \pm 2\ldots$ is the magnetic quantum number as referenced with respect to the static field axis. After plugging $\psi(\mathbf{r})$ into the Schrödinger equation we are left with two

decoupled differential equations for the wavefunctions X and Y. These equations contain the separation constants Z_1 and Z_2, respectively, with $Z_1 + Z_2 = Z$. The electron may be ionized solely along the υ-coordinate. Therefore, one deals with a scattering problem which is solved for given sets of m, F and energy E. In the present work we are interested in the energy range $E \geqslant E_{\rm sp}$ (with $E_{\rm sp} = -2[ZF]^{1/2}$ a.u. the saddle point energy [24]), which includes the zero-field ionization threshold, $E = 0$, as well as the near-threshold positive energy range.

The electron is bound along the χ coordinate and the associated demand $X(\chi \to \infty) \to 0$ leads to the quantization of Z_1. For each eigenvalue $Z_1^{n_1,|m|}$ the corresponding wavefunction $X_{n_1,|m|}$, is characterized by its n_1 nodes. On the other extreme, the small-χ asymptotic behavior of X is,

$$\underset{\chi\to 0}{X(\chi)} \to A_X \chi^{|m|+1/2}\left[1 + O\left(\chi^2\right)\right] \tag{1}$$

where A_X>0 is a normalization constant that is a slowly decreasing function of energy and becomes practically zero for $Z_1(E)$<0.

The small-υ asymptotic behavior of wavefunction Y is quite similar to that of X in equation (1). For $\upsilon \to \infty$, however, the asymptotic form of Y writes,

$$\underset{\upsilon\to\infty}{Y} \propto \frac{1}{k^{1/2}(\upsilon)} \sin\left[\theta(\upsilon) + \phi\right], \tag{2}$$

with

$$k(\upsilon) = \left[F\upsilon^4 + 2\mathrm{E}\upsilon^2 + 4Z_2 - \frac{\left(4m^2 - 1\right)}{4\upsilon^2}\right]^{1/2}, \tag{3}$$

the wavenumber function. As for the phase θ, it is given by

$$\theta(\upsilon) = \int_{\upsilon_o}^{\upsilon} k(\upsilon')\,\mathrm{d}\upsilon', \tag{4}$$

while ϕ is a constant phase depending on υ_o.

The experimentally recorded quantity of interest here is the outgoing flux of ionized electrons, as given by the probability current density $J_{\upsilon_{\rm det}}(\phi,\rho)$, along a paraboloid of constant $\upsilon = \upsilon_{\rm det}$ [9]. For sufficiently large $\upsilon_{\rm det}$ and for the range of importance of the values of the electron impact radius $\rho = \chi\upsilon_{\rm det}$, this paraboloid practically coincides with the plane of the PSD which is perpendicular to z-axis and located at $z_{\rm det} = -\upsilon^2{}_{\rm det}/2$. The glory signal $J_{\rm Glory}$ corresponds to the center of each $J_{\upsilon_{\rm det}}(\phi,\rho)$ image, that is $J_{\rm Glory} \equiv J_{\upsilon_{\rm det}}(\phi, \chi = \rho = 0)$. From the asymptotic small-χ behavior of equation (1) it turns out that only $m = 0$ states may exhibit non-zero signal at $\rho = 0$ and thus only these states contribute to the formation of the glory signal, which is written as [11],

$$J_{\rm Glory} \propto \left|\sum_{n_1} d_{n_1,0} A_{X,n_1,0} e^{\mathrm{i}\left[\theta_{n_1,0}(\upsilon_{\rm det}) + \phi_{n_1,0}\right]}\right|^2. \tag{5}$$

The quantities $d_{n_1,m} = \left\langle \psi^{E,F}_{n_1,m} \middle| \hat{\mathrm{T}} \middle| \psi_i \right\rangle$ in equation (5) stand for transition matrix elements between the initial state ψ_i and final Stark states $\psi^{E,F}_{n_1,m}$, with $\hat{\mathrm{T}}$ denoting the relevant transition operator (here either the single- or two-photon dipole one).

Since experimental glory recordings with high spectral resolution and over a wide energy range are time consuming, it is quite difficult to eliminate small gradual drifts of laser pulse energy with time. Therefore, to avoid intensity variations of $J_{\rm Glory}$ caused by these drifts, instead of the glory signal alone, the ratio between $J_{\rm Glory}$ and the total ionization cross section $\sigma_{\rm tot}$ is preferred instead [11]. Theoretically, $\sigma_{\rm tot}$ is obtained by integrating over the whole surface of the detector and it is proportional to the incoherent sum over the squared matrix elements,

$$\sigma_{\rm tot} \propto \sum_{n_1,m} |d_{n_1,m}|^2. \tag{6}$$

The numerator and denominator of the scaled glory signal, $J_{\rm Glory}/\sigma_{\rm tot}$, should both refer to the same Stark states. Given that $J_{\rm Glory}$ probes solely the $m = 0$ ones, measurements and calculations of the present work are performed for linear laser polarization parallel to the direction of the electric field (dipole transitions selection rule $\Delta m = 0$/per photon and excitation out of an $m = 0$ initial state). Details on the computation of all the above presented quantities may be found in [9].

Let us now extend our discussion to multi-electron atoms, dealing particularly with a highly excited (Rydberg) electron outside a generally sizable $Z = Z_{\rm eff}$ ionic core, that differs from a point-like positive charge. Then, according to FTT [18–20], the central equations (5) and (6) remain formally unchanged, but there are important differences regarding the transition matrix elements, which are now decomposed as,

$$d_{n_1,m} = \sum_{\ell} d^m_\ell a^m_{\ell,n_1} \tag{7}$$

with d^m_ℓ the zero-field excitation matrix elements. In equation (7) ℓ denotes the orbital angular momentum quantum number and the relevant sum runs over all its final state values that are permitted by the selection rule $\Delta\ell = \pm 1$/per photon. As for the factors a^m_{ℓ,n_1}, they are given by

$$a^m_{\ell,n_1} = \sum_{n'_1} W^m_{\ell,n'_1} B^{|m|}_{n'_1,n_1}, \tag{8}$$

and they depend on the elements of the matrices $\mathbf{W}$ and $\mathbf{B}$ [20] written as,

$$\mathbf{B}^{|m|} \equiv \left[\mathbf{I} - \mathrm{i}\mathbf{R}^{|m|}\right]^{-1}, \tag{9}$$

and

$$\mathbf{W}^m \equiv \cos\delta^{-1}\left[\mathbf{U}^m\right]^T \left[\mathbf{I} - \cot\gamma^{|m|}\,\mathbf{K}^{|m|}\right]^{-1}, \quad \mathbf{W}^{-|m|} = (-1)^{|m|}\mathbf{W}^{|m|}. \tag{10}$$

In equations (9) and (10), **I** is the identity matrix, **R** the, so-called, reaction matrix,

$$\mathbf{R}^{|m|} = \mathbf{K}^{|m|}\left[\mathbf{I} - \mathbf{cot}\gamma^{|m|}\,\mathbf{K}^{|m|}\right]^{-1} \tag{11}$$

and

$$\mathbf{K}^{|m|} = \mathbf{U}^{m}\,\mathbf{tan}\delta\,\left[\mathbf{U}^{m}\right]^{\mathrm{T}} \tag{12}$$

(superscript T denotes transposition). The frame transformation matrix **U** (with $\mathbf{U}^{-|m|} = (-1)^{|m|}\mathbf{U}^{|m|}$) connects the Stark parabolic channels with the spherical, zero-field, ones near the ionic core where the potential energy generally deviates from the pure Coulomb potential, but it is assumed to be spherically symmetric [18, 19]. Furthermore, the diagonal matrix $\mathbf{cot}\boldsymbol{\gamma}^{|m|}$ is of hydrogenic origin and reflects the n_1-specific large-υ relative phase $\gamma_{n_1}^{|m|}$ between hydrogenic regular and irregular Y-wavefunctions. This implicitly assumes that the small-υ regular and irregular Y-wavefunctions are phase lagged by $\pi/2$ [19]. This definition differs from that employed in standard scattering theory, were the $\pi/2$ phase lag is imposed at large distances. Finally, the two diagonal matrices, $\mathbf{cos}\boldsymbol{\delta}$ and $\mathbf{tan}\boldsymbol{\delta}$, are composed by the phases $\delta_\ell = \pi{\cdot}\mu_\ell$, where μ_ℓ are the quantum defects of zero-field Rydberg series. For zero quantum defects we have $\mathbf{R} = \mathbf{K} = 0$ and the theory becomes purely hydrogenic. Non-zero quantum defects in non-hydrogenic atoms stem either from the penetration of the excited, low-ℓ electron wavefunctions into the ionic core, or from the polarization of the core due to the presence of high-ℓ Rydberg electrons. In either case, they can be obtained from experimental data [25].

Equation (9) shows that matrix elements $d_{n_1,m}$ become necessarily complex. Thus, atom-specific phase-shifts are to be expected in equation (5), in addition to the hydrogenic ones $\theta_{n_1,|m|}(\upsilon_{\mathrm{det}}) + \phi_{n_1,|m|}$. Further, it is to be stressed that the interaction between the excited electron and the ionic core implied by non-zero quantum defects causes n_1-channel mixing. This mixing is evident in equation (8) and, therefore, the quantities a^{m}_{ℓ,n_1} may be decomposed into 'mixing amplitudes' between channel n_1 and all channels n_1'.

For obtaining the glory signal we introduce equation (7) into equation (5). For the single-photon excitation of $m = 0$ Stark states out of an $m = 0$ ground state the total cross section writes

$$\sigma_{\mathrm{tot}} \propto \Delta^{0}_{11}, \tag{13}$$

employing the 'density of states' Δ^{0}_{11} [19]. Generally, the quantities $\Delta^{|m|}_{\ell\ell'}$ are defined as

$$\Delta^{|m|}_{\ell\ell'} = \sum_{n_1}\mathrm{Re}\left[a^{|m|}_{\ell,n_1}\left(a^{|m|}_{\ell',n_1}\right)^{*}\right]. \tag{14}$$

In contrast, the absorption of two-photons out of an $m = 0$ ground state leads to ns and nd final zero-field Rydberg states and involves a p-wave virtual intermediate state ($|v\mathrm{p}\rangle$). The two-photon total Stark ionization cross section may then be written as [19],

$$\sigma^{(2)}_{\mathrm{tot}}(E) \propto \Lambda^2\Delta^{0}_{00}(E) + \frac{4}{\sqrt{5}}\Lambda\Delta^{0}_{02}(E) + \frac{4}{5}\Delta^{0}_{22}(E). \tag{15}$$

The dimensionless parameter Λ appearing in equation (15) denotes the relative strength between the *radial* matrix elements [10] corresponding to the transitions $|v\mathrm{p}\rangle \rightarrow |n\mathrm{s}\rangle$ and $|v\mathrm{p}\rangle \rightarrow |n\mathrm{d}\rangle$, respectively.

3. Experimental set-up and procedure

The experimental set up was described in some detail in [9, 11, 26]. Briefly, Sr pellets are sublimated in an electro-heated oven. Strontium vapor escapes from the oven through a small nozzle, forming a thermal atomic beam that enters a laser-atom interaction chamber which is held at a background pressure of $\approx 7 \times 10^{-7}$ mbar. The atomic beam crosses perpendicularly the ionizing laser beam. The latter stems from a pulsed Nd:YAG pumped dye laser that delivers pulses of $\sim$5 ns duration and $\sim$0.2 cm^{-1} linewidth at a 10 Hz repetition rate. The dye laser's fundamental visible radiation (434–437 nm) is frequency doubled (217–219 nm) by a BBO (Beta Barium Borate) crystal and the produced UV radiation is separated from the fundamental by appropriate dichroic filters. A small part of the fundamental beam is sent to a frequency calibration system offering an absolute frequency uncertainty lower than 0.5 cm^{-1}.

Ground state ($5s^2\ {}^1S_0$) strontium atoms are excited (and subsequently ionized) near their first 5s threshold via the absorption of either one-UV-photon or two-visible-photons. In either case the linear polarization of the exciting beam is purified by passing through a Rochon polarizer and accurately set parallel to the static electric field axis by means of an appropriate $\lambda/2$ retarder. With this arrangement only $m = 0$ final Stark states are excited allowing for the emergence of the glory effect. Finally, the laser beam is focused in the vacuum chamber thought a $\approx$ 20 cm focal length lens.

The static electric field is oriented along the axis of the spectrometer, whose laser-atom interaction geometry is the standard one employed in three-electrode velocity-map imaging (VMI) spectrometers [27]. This geometry consists of a solid electrode (the repeller R) and two subsequent electrodes with central apertures (the extractor E and the grounded one G). The atom-laser interaction and photoionization takes place midway between R and E which are held at appropriate voltages V_R and V_E, respectively. The ratio V_E/V_R satisfies the VMI focusing condition [27]. Due to the presence of the apertures in E and G, the produced electric field is inhomogeneous, allowing velocity focusing. If the interaction region is constrained enough, however, this field can be considered as nearly homogeneous. Produced photoelectrons are accelerated by the field and guided to a subsequent field-free drift tube, at the end of which they are detected by a two-dimensional PSD. An electrostatic Einzel lens is placed about halfway through the tube, allowing for magnification of the images by

a factor up to 20 [28, 29]. The entire spectrometer is covered with a double μ-metal layer providing protection from stray magnetic fields. The PSD is made of a tandem microchannel plate assembly and a phosphor screen. A CCD camera records the two-dimensional distribution of light spots on the screen. Recorded images are transferred to a computer, where they are accumulated over several-thousand laser shots.

4. Results and discussion

4.1. General remarks

Near-5s-threshold experimental images from both single- and two-photon excitation of strontium were recorded out of the $5s^2\ ^1S_0$ ground state. As mentioned above, the laser polarization was in either case linear and parallel to the static electric field, leading to the exclusive excitation of $m = 0$ final Stark states, the latter permitting the appearance of the glory effect. The full scan is approximately centered on the $E = 0$ zero-field limit, while its lower energy is $E \approx E_{sp}$. The measurements were stepped at equal intervals of $\Delta E = 0.2\ \mathrm{cm}^{-1}$. Due to this small energy step the experimental procedure involved more than 3000 images and was completed in about a week for each set of a given excitation scheme. Great care was taken in maintaining almost identical experimental conditions. Particularly, the laser pulse intensity was kept within the same limits on a daily basis. These limits were low enough to avoid saturation effects on either the glory signal or the total electron signal, the latter obtained by angularly and radially integrating over the whole detector's surface. Low laser intensity limits additionally prevented detector fatigue and deterioration of its sensitivity in its areas where the electron signal is intense. On the other hand, a small gradual drop of the laser performance was inevitable for each set of measurements. Therefore, as mentioned in the theoretical section, to avoid glory magnitude variations caused by the drift of laser pulse energy, instead of measuring the glory signal itself, we employed the ratio of this signal divided by the total one. In the absence of saturation effects this total signal is proportional to σ_{tot}. It was additionally verified that the so-obtained total ionization cross section closely matches the Sr^+ spectrum recorded by scanning the dye laser frequency, after reversing the polarities of all VMI voltages, turning-off the Einzel lens and using the microscope as a simple time-of-flight spectrometer.

The static field strength was roughly estimated on the basis of the applied voltages, taking into account the geometry of electrodes. Its value was then refined using the lowest energy where the first image was measurable and by means of the energy evolution of the outermost inflection point radius ρ_{ip} of the radial distribution $R(\rho)$ [2, 6, 14, 15, 26]. The latter is obtained by angularly integrating each recorded image. Note that ρ_{ip} is independent of the magnitude of $R(\rho)$ and it is expected to follow closely the maximum classical radius ρ^{cl}_{max} involving E_{sp} [2, 6, 11, 14, 15]. Thus, the saddle point energy and consequently the strength F are estimated by fitting ρ_{ip} to the known formula for $\rho^{cl}_{max}(E)$ [2, 14, 15]. Furthermore, once E_{sp} is known, we may conveniently discuss our findings and compare them with earlier work referring to different static field strengths in terms of the dimensionless reduced energy variable,

$$\varepsilon \equiv \frac{E}{|E_{sp}|}. \tag{16}$$

In our presentation below we examine separately the scaled glory signal (J_{Glory}/σ_{tot}) and the total ionization cross section (σ_{tot}) spectra for the single- and two-photon excitation cases. These data are accompanied by the corresponding theoretically calculated quantities, either for hydrogen atom or for a non-hydrogenic one, simulating the Sr atom. The required field-free $5sn\ell$ Rydberg series quantum defects are obtained from the available spectroscopic data [25, 30]. Specifically, we included $\ell = 0$–9 states and for the near-threshold energy range ($n \geqslant 30$), we employed the quantum defects $\mu_s = 3.27$, $\mu_p = 2.73$, $\mu_d = 1.64$ and $\mu_f = 0.09$. For $\ell > 3$ all quantum defects were set equal to zero. The non-zero quantum defects were transformed for FTT according to the rules given by Harmin [19]. Note that for the $5sn$p states, the quantum defects of the $^1P_1$ series are chosen, which are, however, perturbed by doubly excited states and vary with energy. Here we employ a constant quantum defect corresponding to its 5s-threshold value. Additionally, for the $5sn$d states we preferred the $^3D_2$ series quantum defects, because of the singlet-triplet mixing and reverse of the singlet character in this energy range [30]. As for the field-free dipole matrix elements, there is practically no such information required for the single-photon ionization case (see equation (13)). For the two-photon ionization case, the dimensionless ratio Λ appearing in equation (15) is estimated via the so-called Coulomb approximation [31]. The relevant dipole matrix elements are numerically evaluated between a final Rydberg s- or d-state of energy E_ℓ ($\ell = 0,2$) and a virtual p-state, $|vp\rangle$, of energy $E_v = (E_\ell + E_g)/2$, where E_g is the ground state energy [25]. For estimating E_ℓ we used the aforementioned Rydberg series quantum defects. This resulted to $\Lambda = 0.08$, in accordance with the well-known propensity rules [32] favoring the $|p\rangle \rightarrow |d\rangle$ transition over the $|p\rangle \rightarrow |s\rangle$ ones.

4.2. The single-photon scaled glory signal

The experimental and computed data corresponding to single-photon excitation are presented in figure 1. Beginning with the field strength estimation, figure 1(a) shows the measurements of the outermost inflection point ρ_{ip} as a function of energy E and the $\rho^{cl}_{max}(E)$ [2, 14, 15] curve fitted to them. The obtained E_{sp} value and its uncertainty (given in the plot) result in $F = 860\ \mathrm{V\ cm}^{-1}$ and an uncertainty of $\pm 4\ \mathrm{V\ cm}^{-1}$. This fitted value is fully compatible with the lowest energy where the first image is measurable and the near-E_{sp} behavior of the Sr^+ spectrum given in figure 1(b). However, by including these two additional criteria, we estimate an overall uncertainly that is somewhat increased to $\pm 10\ \mathrm{V\ cm}^{-1}$.

As it becomes obvious from figure 1(b), within the range $-180\ \mathrm{cm}^{-1} \leqslant E < -80\ \mathrm{cm}^{-1}$ ($-1 \leqslant \varepsilon \leqslant -0.45$, see the upper x-axis of figure 1) the σ_{tot} spectrum is dominated by Stark resonances that are, however, superimposed to continua. On

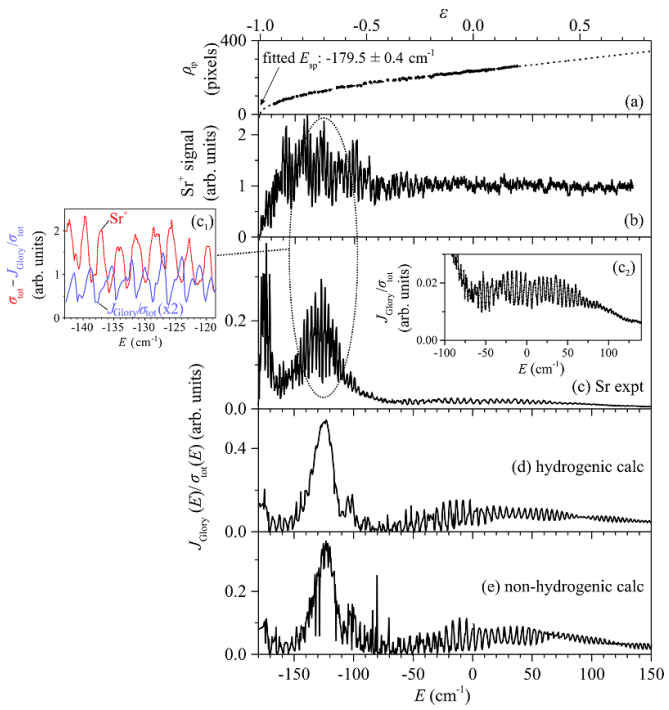

Figure 1. Single-photon near-threshold ionization of ground state Sr atoms under the presence of a static electric field. The laser polarization is linear and parallel to the field axis ($m = 0$ final Stark states). (a) Field strength estimation via the energy evolution of the outermost inflection point radius ρ_{ip} (black circles) of the radial distributions $R(\rho)$ obtained from the recorded images [6, 26]. The dashed line shows the fit of the $-170\ \text{cm}^{-1} < E < 40\ \text{cm}^{-1}$ data set to the maximum classical radius ρ^{cl}_{max}[2, 14, 15]. The fitted E_{sp} value reported in the plot corresponds to a field strength $F = 860 \pm 4\ \text{V cm}^{-1}$ and allows for the energy scale to be expressed in terms of the reduced energy variable ε (upper x-axis). (b) Recorded Sr^+ signal (proportional to σ_{tot}) as a function of excitation energy. (c) Energy dependence of the scaled glory signal, obtained by integrating each experimental image over a radius equal to ∼5% of $\rho_{ip}(E = 0)$ and dividing it by the total electron signal (also proportional to σ_{tot}). Inset (c_1) shows the details of the scaled glory and Sr^+ signals in the vicinity of the local maximum of the former, around $E \sim -127\ \text{cm}^{-1}$ ($\varepsilon \sim -0.71$). Inset (c_2) shows at an enlarged y-scale the scaled glory oscillations observed about the zero-field limit ($E = 0$). (d) Quantum mechanical computation of the scaled glory spectrum corresponding to single-photon excitation of hydrogen atom out of its ground state. (e) The analogous scaled glory computation corresponding to single-photon excitation of a non-hydrogenic atom with zero-field quantum defects (given in the text) that simulate the Rydberg states of Sr.

the contrary, for $\varepsilon > -0.45$ any resonant structure disappears, and the continua completely dominate. In particular, as expected from earlier experimental and theoretical work on Rydberg Stark spectra [19, 24, 33], the average ionization cross-section is constant (i.e. flat) in the vicinity of the zero-field ionization threshold. On the other hand, we do not observe the predicted and occasionally recorded modulations of σ_{tot} within the $E \geqslant 0$ range, these modulations being associated to so-called static field induced states (SFIS [8]). We may anticipate that, due to the low static field value, these modulations are of very low contrast and are thus masked by noise [33]. The situation is quite similar to that of two-photon excitation of Mg [11].

In contrast to the total ionization cross section, the experimental scaled glory spectrum shown in figure 1(c) exhibits rich structure for either negative or positive energy. This structure is subjected to a strong overall modulation which results to three broad lobes. The term 'lobe' refers to the envelope of a gross spectral structure spanning a certain energy range and exhibiting a local signal maximum. Each lobe may include oscillating substructures of appreciable amplitude, as well as locations of minimum oscillation amplitude due to destructive interferences caused by beating effects. The first lobe spans the range $E_{sp} \leqslant E \leqslant \sim$–165 cm^{-1} (–1 $\leqslant \varepsilon \leqslant \sim$–0.92), i.e. practically appears at the saddle point energy. Its high intensity is attributed to the quite small experimental value of σ_{tot} at this energy range. This local maximum is classically expected [14]. The second, somewhat weaker, lobe spans the range $\sim$–160 cm$^{-1} \leqslant E \leqslant \sim$–100 cm^{-1} ($\sim$–0.89 $\leqslant \varepsilon \leqslant \sim$–0.56). Its local maximum appears at $\varepsilon \sim$ –0.71, that is close to the so-called direct limit $\varepsilon_{dir} \approx -0.775$ (above which the first glory angle becomes meaningful, while $\beta_0(\varepsilon_{dir}) = \pi$) [2]. This lobe, as well as the fact that it is located at somewhat higher energy than ε_{dir}, is also classically expected [14]. Finally, the third, hardly visible, lobe spans the range $\sim$–70 cm$^{-1} \leqslant E \leqslant \sim$+80 cm^{-1} ($\sim$–0.4 $\leqslant \varepsilon \leqslant \sim$+0.45) and it is centered at $\varepsilon \sim 0$. This last lobe is not predicted classically, but it results from beating effects emerging from the coherent n_1-summation in equation (5) and is discussed in more detail below. It is interesting to note that the overall envelope differs from that recorded in Mg [11].

The structure within each lobe consists of high periodicity oscillations. The negative energy ones bear a connection with the Stark resonant structure also appearing in σ_{tot}. However, the importance of resonances is minimized in the quantity J_{Glory}/σ_{tot} as compared to the undivided glory signal J_{Glory} [9, 11] and, therefore, the oscillations observed in figure 1(c) are not to be solely attributed to resonances. Indeed, while a clear correspondence can be found in figure 1(b) for most of the scaled glory oscillations near $\varepsilon = -1$ and up to $\varepsilon \sim$ –0.84, this is not the case for the intermediate glory lobe at $\varepsilon \sim$ –0.71. There, an apparent double peak scaled glory structure is observed, which is additionally almost completely out of phase with the single-peak modulations appearing in σ_{tot} (see inset (c_1) of figure 1(c)).

Finally, the high periodicity structure exhibited by the J_{Glory}/σ_{tot} curve in the energy range around $\varepsilon \sim 0$ cannot be associated with resonances, since the Sr^+ signal is practically flat and structureless in this range. In fact, the aforementioned lobe centered at $\varepsilon \sim 0$ has clearly the form of a beating pattern characterized by the two lowest energy locations of minimum oscillation at $\varepsilon \sim$ –0.39 ($E \sim$ –70 cm^{-1}) and $\varepsilon \sim$ –0.19 ($E \sim$ –35 cm^{-1}) and a highest point at $\varepsilon \sim$ +0.45 ($E \sim$ +80 cm^{-1}) where the oscillations amplitude is minimized again (see inset (c_2) of figure 1(c)). From that point on, the scaled glory signal still oscillates but its overall intensity gradually drops further and does not rise again. Furthermore, as expected, the periodicity of the recorded oscillations within this lobe varies with energy. For $\varepsilon > 0$ it increases continuously (like the behavior observed in [11]), while for $\varepsilon \leqslant 0$ does not vary monotonically. Specifically, it is initially increasing from $\varepsilon \sim$ –0.39 and

up to $\varepsilon \sim 0$ and then it appears to decrease for a small number of oscillations before increasing again.

Let us now compare the experimental scaled glory curve of figure 1(c) with the computed hydrogenic one of figure 1(d), corresponding to single-photon near-threshold excitation of final $m = 0$ Stark states out of the 1s ground state and for the same field strength of 860 V cm^{-1}. We first remark that the overall envelope of this glory curve resembles the experimental one, while it is fairly different from that reported for the hydrogenic computation for the two-photon excitation case [11]. Local maxima are observed at $\varepsilon \sim -1$ and $\varepsilon \sim -0.69$, but, in contrast to the experimental curve, the first one is less intense than the second, the latter being additionally less broad than the corresponding experimental one. Moreover, these two negative energy lobes are characterized by the absence of substantial oscillating structures. The reason is not very clear, although the same holds for the total ionization cross section as well. By locally decreasing the energy step by factors 2–10, we are confident enough that this absence of substantial structure is not due to an insufficiently small energy step. Nevertheless, such structures are more visible outside these lobes, particularly the one centered on $\varepsilon \sim 0$. Thus, this third local maximum is centered on the same energy as the experimental one. Another common feature between hydrogenic theory and experiment is the glory cancelation that occurs at $\varepsilon \sim -0.39$ ($E \sim -70$ cm^{-1}) in both curves. In general, the $\varepsilon \geqslant 0$ oscillating patterns bear a close shape resemblance and share the same periodicity. Starting from $\varepsilon \sim -0.3$ ($E \sim -50$ cm^{-1}) where the two signals are somewhat out of phase, they gradually become completely dephased at the positive energy side. Finally, among the remaining differences between the two curves we note the much higher oscillation contrast and the somewhat richer partial beating cancellation structures of the hydrogenic one.

Let us conclude the discussion on the single-photon scaled glory data by commenting on the curve computed by means of the non-hydrogenic theory. We restate that the aforementioned quantum defects for the Sr atom are the only atom-target-specific data required by FTT for the single-photon excitation scheme [19]. The computed $J_{\mathrm{Glory}}/\sigma_{\mathrm{tot}}$ curve is given in figure 1(e) and its resemblance with the curve obtained by the hydrogenic theory is remarkable. The overall envelope and lobes look almost identical. Among the differences, we may first note the much richer oscillating structure within the lobe peaking at $\varepsilon \sim -0.69$, thus resembling more the experimental curve. This apparently 'additional' structure (with respect to the hydrogenic curve) is to be attributed to the coupling between quasi-bound Stark states and continua occurring in multi-electron atoms. This coupling most frequently broadens the resonances [19], which are then easier to emerge for a given computational energy step. However, the most important difference between the two computed curves is that for $\varepsilon \geqslant -0.3$ and particularly for the positive energy range they are almost completely out of phase. This is undoubtedly due to the aforementioned extra phase factors in equation (5) emerging from the target-atom-specific quantum defects. Thus, the inclusion of the quantum defects results in this case to experimental and computed non-hydrogenic scaled glory curves that exhibit in-phase oscillation at positive energies. Another consequence of the quantum defects, but of somewhat lesser importance, refers to the slightly different beating structure between the hydrogenic and non-hydrogenic calculations at positive energies. Finally, the detailed comparison of periodicities between experimental and calculated curves will be discussed below in connection with the STFTs of these curves.

4.3. The two-photon scaled glory signal

The measurements and calculations relevant to two-photon excitation are given in figure 2. The fit of $\rho_{\mathrm{ip}}(E)$ to the $\rho^{\mathrm{cl}}_{\mathrm{max}}(E)$ curve (figure 2(a)) reveals a slightly lower field strength with respect to the one-photon case. This strength is again quite compatible with the near-saddle point two-photon ionization Sr^+ spectrum given in figure 2(b), as well as with the lowest energy where image recordings were quantifiable. This array of measurements finally results to $F = 840 \pm 10$ V cm^{-1}. Thus, taking into account their uncertainties, the field strengths for the one- and two-photon cases almost overlap. The small difference is probably due to a small displacement of the visible laser beam with respect to the UV beam along the spectrometer axis.

Contrary to the single-photon excitation, the spectrum of figure 2(b) is dominated by Stark resonances only up to $\varepsilon \leqslant -0.6$ and there is apparently less resonant structure. For higher excitation energy only structureless continua are observed. Furthermore, for $\varepsilon \geqslant 0$, resonances due to SFIS [33] are once more not detected, as they are probably masked by noise due to their small amplitude. This situation is similar with the one shown in figure 1(b) and with earlier observations in Mg [11].

The scaled glory spectrum of figure 2(c) exhibits the expected gross structure of classical origin with two lobes centered at $\varepsilon \sim -1$ and $\varepsilon \sim -0.7$, respectively. The former lobe is the one of higher intensity and modulated due to the resonant Stark structure near E_{sp} that is also observed in figure 2(b). Distinctive modulations which are not solely due to resonances are evident also within the second lobe, along with a characteristic dip at $\varepsilon \sim -0.68$. This dip is absent in the single-photon scaled glory spectrum (figure 1(c)) but it was already observed in the corresponding two-photon one of Mg [11]. The latter spectrum was found to additionally exhibit an accompanying consecutive local minimum due to beating effects. Such a local minimum is also observed in figure 2(c) at $\varepsilon \sim -0.55$, but faintly, since it is much weaker and less pronounced than that in the Mg curve. We may conclude that, apart from its features of classical origin, the gross structure of the scaled glory curve characterizes the two-photon excitation scheme, but the fine details of the overall envelope are target-atom specific.

Apart from the features discussed above there are other weaker ones due to beating cancellations, resulting in local minima at $\varepsilon \approx +0.17$ ($E \approx +30$ cm^{-1}) and $\varepsilon \approx +0.73$ that enclose a lobe exhibiting a local maximum around $\varepsilon \approx +0.45$ ($E \approx +80$ cm^{-1}). This last positive energy maximum is modulated by high periodicity oscillations, whose contrast

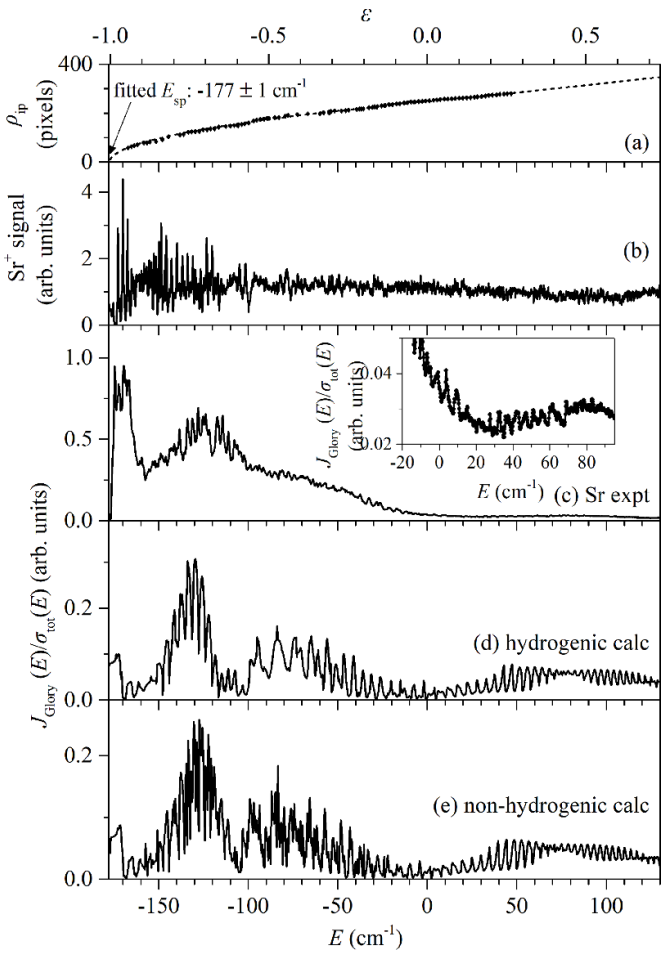

Figure 2. Same as in figure 1 but for the case of two-photon near-threshold ionization of ground state Sr atoms under the presence of a static electric field. In (a) the fit of the $-170\ \text{cm}^{-1} < E < 50\ \text{cm}^{-1}$ data set of ρ_{ip} (black circles) to ρ^{cl}_{max} resulted to the reported E_{sp} value (employed for the upper x-axis) and to the value $F = 840 \pm 10\ \text{V cm}^{-1}$. In (e), apart from the zero-field quantum defects, the non-hydrogenic scaled glory computation additionally requires the relative strength Λ between *radial* matrix elements corresponding to the transitions $|\nu p\rangle \rightarrow |ns\rangle$ and $|\nu p\rangle \rightarrow |nd\rangle$, respectively ($|\nu p\rangle$ denotes the p-wave virtual state's wavefunction—see theoretical section). The value employed in the calculation is provided in the text.

with respect to the underlying background signal is much weaker (in fact, they are barely observable) as compared to the single-photon case. We may anticipate that the overall absence of considerable structure and the very weak contrast of the recorded oscillations in the two-photon data may be partially attributed to the much lower signals (with respect to the single-photon case), resulting to a decreased signal-to-noise ratio.

Finally, the theoretical hydrogenic and multielectron scaled glory curves are plotted in figures 2(d) and (e), respectively. The overall envelopes of these curves are almost identical, having in particular the signal cancelations due to beating at exactly the same locations. They also bear a close resemblance to the hydrogenic two-photon curve given in [11] that was computed for a different field strength. Nevertheless, with respect to that curve, the presently computed ones mainly differ in contrast and intensity of the positive energy oscillations, as compared to their negative energy signal magnitude. Furthermore, the curves (d) and (e) of figure 2 exhibit positive energy oscillations that are practically identical in both location and contrast. However, the negative energy parts of the curves differ in that the multi-electron one exhibits much more structure within the gross lobes with respect to the hydrogenic curve. This is a common feature with the single-photon excitation case above, where it is attributed to the coupling between continua and quasi-bound states. Additionally, while a small split of the main lobe around $E \sim -130\ \text{cm}^{-1}$ is barely observable (and absent in the hydrogenic counterpart curve), it resembles the dip observed in the experimental curve of figure 2(c). Furthermore, the $\varepsilon \geqslant 0$ oscillating patterns of theory and experiment share the same periodicity. Apart from these similarities, however, both model calculations markedly differ from the experimental curve in the contrast of their glory oscillations with respect to the overall magnitude over the whole examined energy range, as well as the degree and depth of beating cancellations. This is particularly evident in the cancelation around $\varepsilon \sim -0.55$, which is present in both theory and experiment. Additionally, the $\varepsilon < 0$ detailed structure of the theoretical curves (particularly the non-hydrogenic one) appears to be much richer than that of the experimental scaled glory curve. Note that the calculations are performed with the experimental energy step, but are not convoluted with the effective two-photon laser linewidth. Let us finally mention that the experimental positive energy, high-periodicity oscillations become alternatively in phase and out of phase with the ones of the computed curves (the latter also exhibiting the same behavior). Considering the single-photon excitation case, where the experimental positive energy oscillations and those calculated via the non-hydrogenic model are found to be in phase, the above dephasing in the two-photon ionization case should probably be attributed to the employed value of the parameter Λ.

4.4. STFTs of scaled glory spectra

As pointed earlier in [11], a more systematic examination of the periodicity variations exhibited by the scaled glory signal at several distinct energy ranges necessitates the use of 'short time Fourier transform'. Indeed, STFT is most frequently applied for analyzing time-signals characterized by a time-varying frequency and phase [16]. A selected window function moves along the time axis and the Fourier transform is applied solely within this window. Artifacts at the boundaries are avoided by choosing an appropriate window shape and by allowing the overlapping between successive windows. In the present work, a Blackman window function is chosen [34] and the overlap between adjacent energy windows was set to be comparable to the window width. The procedure leads to a two-dimensional representation of the frequency content as a function of time. Of course, in our case the two conjugated variables are still time and frequency (energy), but they are interchanged. Nevertheless, the frequency-time transformation still implies that the spacing ΔE, of the glory oscillations

is related, at least locally, to the characteristic difference time peaks Δt via $\Delta E{\cdot}\Delta t = 2\pi$ (in atomic units).

At $E \geqslant 0$ the observed energy periodicity of the scaled glory signal is somewhat higher than that reported in [11] for the Mg atom. This is to be expected because the present field strength is also somewhat higher (expected scaling $\propto F^{1/4}$ [11]). Nevertheless, the two periodicities are comparable. Therefore, we adopt the same energy window width of ≈20 cm^{-1}, which appears suitable, at least for positive energy, and corresponds to a time uncertainty of ≈1.5 ps. The obtained two-dimensional STFT representations for the full energy range of the experimental and computed, scaled, single-photon excitation glory spectra of figure 1 are given in figure 3. Likewise, figure 4 shows the STFT representation of the experimental and computed data of figure 2 corresponding to two-photon excitation. To establish a unified presentation, the x-axes of both figures 3 and 4 refer to the dimensionless reduced energy variable ε (equation (16)), computed using the fitted saddle point energy corresponding to each case. Furthermore, the y-axes are expressed in terms of the 'universal' scaled quantity $F^{3/4}t$ (in atomic units), allowing for a comparison between glory data referring to different field strengths [22]. Nevertheless, the right y-axes of figures 3(a) and 4(a), showing the STFTs of the experimental data, are expressed in actual time units (ps) and are specific to each figure. Furthermore, for bringing out the important, albeit weak, features of the plots a logarithmic color scale is employed for the STFT amplitudes. Finally, along with the experimental or quantum results, superimposed on the plots are the scaled versions, $F^{3/4}\Delta t(\varepsilon,\beta_k)$, of the relevant classical, time-delay curves [11],

$$\Delta t\,(\varepsilon,\beta_k) = \mathrm{ToF}\,(\varepsilon,\beta=\beta_k) - \mathrm{ToF}\,(\varepsilon,\beta=\pi)\,. \qquad (17)$$

Equation (17) describes the time-delays as differences between times-of-flight (ToFs) of source-to-detector trajectories corresponding to given pairs of ejection angles β. Specifically, each time-delay is defined as the ToF difference between the trajectory corresponding to a given glory angle β_k, k =0,1,2… (for which the electron ends up at the image center) and the simplest reference straight line trajectory for $\beta = \pi$, i.e. for electron ejection towards the detector and opposite to the field direction. It is important to stress that the connection between the time difference Δt and the periodicity of the glory structures with excitation energy are related to the classical action S along the two interfering trajectories via the relation $\Delta t = \partial S/\partial E$ [11]. All classical calculations refer to $m = 0$ where planar electron motion applies. The initial electron position is set at the origin of the reference system and the initial momentum is given by energy conservation. Thus, once the field strength is fixed, a given origin-to-detector trajectory and its ToF are completely determined by the excitation energy E and the ejection angle β [2, 14, 15].

As a first remark on the plots of figures 3 and 4, we note that they all show a horizontal and intense branch at $t = 0$ and all along the energy axis. As mentioned in [11], this 'DC'

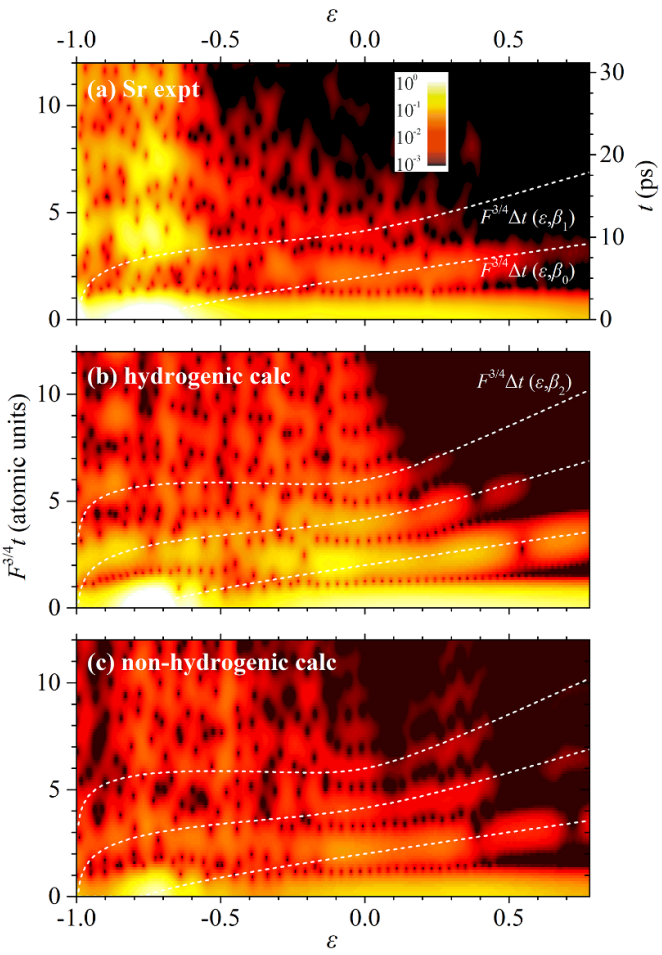

Figure 3. Short time Fourier transforms (STFTs) of the single-photon excitation scaled glory spectra given in figure 1. Specifically, the STFTs refer to the experimental Sr (a), computed hydrogenic (b) and computed non-hydrogenic (c) scaled glory spectra, the latter two calculated as described in the text. The x-axis refers to the dimensionless reduced energy variable ε, for the computation of which the fitted E_{sp} value given in figure 1(a) is used. The y-axes are expressed in terms of the 'universal' scaled quantity $F^{3/4}t$ (in atomic units) which allows for comparison between glory data referring to different field strengths [22]. Only the scale of the right y-axis of (a) is expressed in actual time units (ps) that are relevant to the specific field strength $F = 860$ V cm^{-1}. Drawn with white dashed lines in (a), (b) and (c) are the classically computed [11, 22] differences $\Delta t(\varepsilon,\beta_k)$ between the arrival times on the detector for the electron trajectories ending up to the image center and corresponding to launch angle $\beta = \pi$ and glory angles β_k, for $k = 0$, 1, 2 (see equation (17)). The moving STFT window is of the Blackman type [34]. Its width is ≈20 cm^{-1} ($\Delta\varepsilon \approx 0.1$), leading to a time resolution of ≈1.5 ps ($F^{3/4}\Delta t \approx 0.64$ atomic units). To reduce artifacts at the boundaries, the overlap between adjacent energy windows is set to be comparable to their width. Finally, the logarithmic color scale given in (a) is common to all plots and covers three orders of magnitude.

Fourier component of the STFT plots represents the energy variation of the average value of the scaled glory signal within the moving window. In the absence of quantum effects we would expect this energy variation to reproduce the classical scaled glory curves [14]. However, as revealed by the present

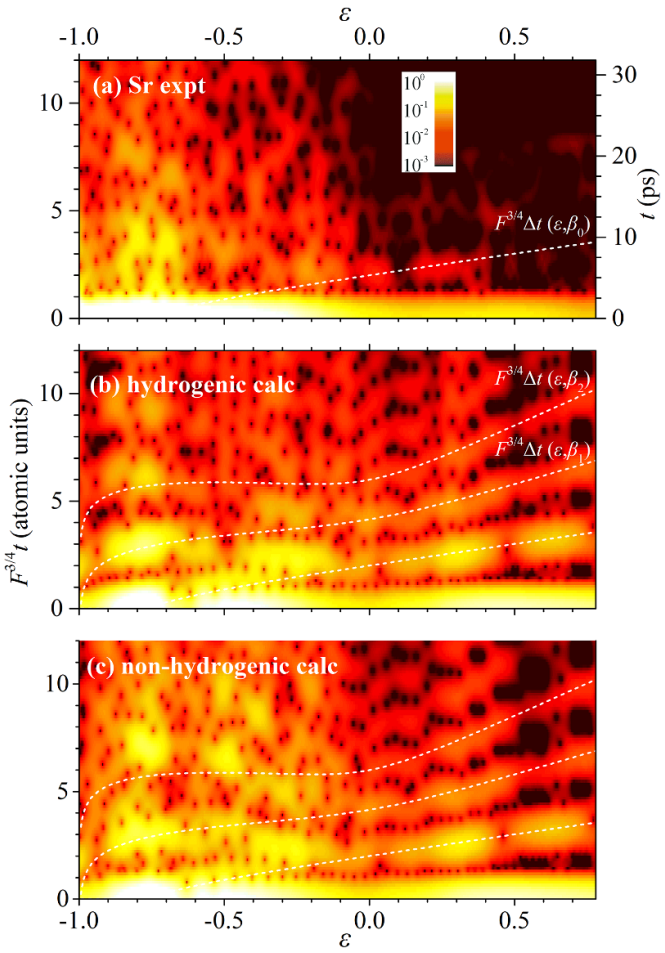

Figure 4. Same as in figure 3, but for the STFTs of the two-photon excitation scaled glory spectra given in figure 2. All STFT parameters reported in figure 3, apply here as well.

experimental study and calculations (see figures 1 and 2), they also reflect effects of quantum origin, namely the gross beating and signal cancelation behavior of the glory spectra. Hence, the shapes of these average signals (or 'envelopes') carry more information than their 'universal' classical counterparts, as they additionally depend on the excitation scheme.

Further, the representations of the theoretical data (figures 3(b), (c) and 4(b), (c)) include the $k = 0$–2 classical $F^{3/4}\Delta t(\varepsilon,\beta_k)$ curves. For the representation corresponding to the experimental single-photon excitation glory spectrum (figure 3(a)) only the $k = 0,1$ curves are included, since the $k = 2$ component is not observed. As for the representation of experimental two-photon glory spectrum (figure 4(a)), even the $k = 0$ component is rather faint and only this classical curve is drawn. Focusing particularly on the $\varepsilon \geqslant 0$ range, we observe an excellent matching between either experimental or theoretical STFT representations on the one hand and the $F^{3/4}\Delta t(\varepsilon,\beta_k)$ curves on the other. This excellent agreement is a formidable illustration of the correspondence principle. The latter is here applied in a relatively complex concrete case where no fixed frequency is defined, and where information of 'spectroscopic' nature (whose existence is intrinsically linked to the presence of the DC-field, and which has no counterpart when this field is deactivated) provides detailed and quantitative information about the underlying classical dynamics in a quantum system in interaction with its environment. To our knowledge, there is no equivalent in the literature of such a striking correspondence between quantum system and classical dynamics in the case of non-periodic continuum orbits that result in quasi-quantization in the ionization continuum. This is a common feature with the earlier Mg experiment [11] and proves the robustness of this quite interesting positive energy structure of the glory spectrum and its STFT representation. In fact, the structure proves to persist for different atoms and excitation schemes, as demonstrated by the earlier and present experimental data and either hydrogenic or non-hydrogenic calculations. Hence, at this energy range differences among representations refer only on rather minor effects, such as the location of energy points of signal cancelation (also observable in the glory curves themselves), and the intensity of each branch or parts of it.

In the positive energy range the $F^{3/4}\Delta t(\varepsilon,\beta_{k>0})$ curves appear to be multiples of the $F^{3/4}\Delta t(\varepsilon,\beta_{k=0})$ one and this leads to relatively regular glory oscillations. By contrast, in the negative energy range these classical curves are distinctly different and no longer multiples of one another, leading to the expectation of a more complex modulation of the glory signal. Indeed, a simple examination of the different spectra in the negative energy range shows no obvious regularity (albeit some structures appear to be piecewise regular). However, the $\varepsilon \leqslant 0$ patterns observed in the STFT representations of figures 3 and 4 exhibit deviations from the $F^{3/4}\Delta t(\varepsilon,\beta_k)$ curves. Stated differently, it is not always evident which features of the representation are associated with a given classical curve. Particularly, within the $-0.5 \leqslant \varepsilon \leqslant 0$ range these deviations include the non-monotonicity and the local minimum of the glory periodicity mentioned in the experimental glory spectrum of figure 1(c). This is common in most theoretical results, but more clearly observed in the representations of the hydrogenic data. In the non-hydrogenic calculations it is somewhat fainter but still visible. What is even more interesting, however, is that these extrema characterize patterns which simply appear as continuations of the positive energy branches to the negative energy range. The patterns (and not only a simple periodicity local minimum) are also present, albeit faint, in the experimental representation of the single-photon excitation case. Thus, the aforementioned 'universality' of these branches appears to concern their full (positive and negative) energy range, despite the fact that the classical $F^{3/4}\Delta t(\varepsilon,\beta_k)$ curves fail to accurately characterize the $\varepsilon \leqslant 0$ part. It is not clear yet, if these negative energy parts are linked with other pieces of time-information related to the classical electron motion. Still, we may exclude with enough confidence the involvement of resonances in these structures. Similarly, as noted above, even for $\varepsilon < -0.5$, and particularly in the neighborhood of the structured local maximum of classical origin at $\varepsilon \sim -0.7$, the involvement of resonances in the scaled glory signal is limited. On the other hand, the strong oscillating

structures occurring within the lobe of this $\varepsilon \sim -0.7$ local maximum, lead to the emergence of certain 'frequencies', appearing as regions of particularly high intensity along the y(time)-axis of the STFT representations. This is evident in both the theoretical and experimental representations and for either case of single- or two-photon excitation. However, a meaningful comparison between theory and experiment appears to be difficult at present, mainly because the experimental data and the non-hydrogenic calculations exhibit somewhat different 'frequencies'. Apparently, the non-hydrogenic model as formulated in this work is rather simplistic and/or the parameters introduced for simulating Sr atom need to be refined. Most probably, however, the two-valence electron character of Sr atom needs also to be considered.

5. Synopsis and outlook

We have presented experimental measurements on the energy variation of the glory signal at the center of slow photoelectron images, obtained by either one- or two-photon near-threshold ionization of ground state Sr atoms in the presence of a static electric field. The resonant Stark structure in the total ionization cross sections, $\sigma_{\rm tot}$, has been found to be different for single- and two-photon excitation. In either case, Stark resonances are only evident near the saddle point energy, while at higher energy and above the zero-field threshold, the ionization spectra are practically structureless. Even more, the influence of resonances on the glory signals is further minimized by dividing (scaling) them by $\sigma_{\rm tot}$ to diminish systematic errors during data acquisition. Despite this minimal contribution from the resonances, each ionization scheme has resulted to scaled glory spectra exhibiting resonant-like structures with electron excitation energy. These resonant-like oscillations are modulated by the classically expected local maxima and by quantum beating effects. Due to the latter effects, the overall gross modulation that envelopes the glory curves has been found to depend sensibly on the excitation scheme. Moreover, judging from the results of an earlier work devoted to two-photon threshold ionization of Mg atom [11], these envelopes also show a target-atom-specific behavior.

We have found that above the zero-field limit the periodicity of the observed glory oscillations increases monotonically with energy. This variation is accurately reproduced by quantum (either hydrogenic or non-hydrogenic) calculations. These results are also in perfect agreement with classical (atom- and excitation scheme-independent) ToFs differences corresponding to pairs of electron trajectories leading to the center of the photoelectron image (classical time-delay curves). These observations confirm those of the Mg study [11] and have thus been proved to be of quite global character. They illustrate strikingly the correspondence principle under a rather complex situation where classical frequency increases with energy, and may moreover be entirely controlled by an external parameter (the strength of the DC field).

Below the zero-field limit ($\varepsilon < 0$) the experimental, two-photon ionization, scaled glory curve shows very little structure, in contrast to the one corresponding to single-photon ionization. Within this negative energy interval the latter curve exhibits a range where the periodicity presents a minimum. This non-monotonic periodicity and its variation with energy are well reproduced by quantum calculations, but not predicted by the aforementioned classical time-delay. Hence, the connection of this behavior with the classical electron motion needs to be explored further.

Finally, while quantum calculations do reproduce the overall structure and oscillation periodicity of the scaled glory spectra, it is evident that this reproduction could benefit from major improvements. Some discrepancies between experimental data and hydrogenic computations can be acceptable, particularly in the negative energy range, since they refer to different atoms with different initial and virtual states and Stark resonant structures. One, however, would expect a better match between experiment and non-hydrogenic computations, the latter including the atom-specific quantum defects and, especially for the two-photon case, an estimate for the relative $\rm p \rightarrow d/p \rightarrow s$ excitation strength. However, one should keep in mind that, as formulated in the present work, FFT is strictly applicable to the Alkali atoms having a single (and here spinless) valence electron outside closed (sub)shells [19]. Instead, Sr atom has two valence electrons outside closed (sub)shells. Nevertheless, since its $5sn\ell$ bound Rydberg states are characterized by a 5s shell which is open but spherically symmetric, the employed FTT can be approximately applied, in principle. On the other hand, Sr is additionally a rather heavy atom where usually different coupling schemes apply for different energy ranges and important configuration interaction occurs even close to the first $5s_{1/2}$ threshold. This, for example, disturbs the $5snp$ series and causes singlet-triplet mixing among the $5snd$ $^{1,3}D_2$ series [30]. Thus, the details of the energy level structure and the (zero-field) symmetry of the states involved cannot be totally ignored. More rigorous FTT treatments are indeed available [35–37] and need to be applied for a better comparison with experiment. Of course, it would be highly instructive to explore the predictions of the present non-hydrogenic model and compare them with relevant experimental data, for a number of Alkali atoms.

Data availability statement

The data cannot be made publicly available upon publication because they are not available in a format that is sufficiently accessible or reusable by other researchers. The data that support the findings of this study are available upon reasonable request from the authors.

Acknowledgments

The authors would like to thank F Lépine for his invaluable comments and suggestions. The experiment was performed at the Central Laser Facility of the University of Ioannina. Technical assistance from E Dimitriadis is gratefully acknowledged.

ORCID iD

S Cohen https://orcid.org/0000-0003-4231-238X

References

[1] Feng Y H, Lei W, Jun L X and Ping L H 2011 *Chin. Phys.* B **20** 063203
Chen Q and Wang D 2015 *Phil. Mag.* **95** 3712
[2] Bordas C 1998 *Phys. Rev.* A **58** 400
[3] Nicole C, Sluimer I, Rosca-Pruna F, Warntjes M, Vrakking M J J, Bordas C, Texier F and Robicheaux F 2000 *Phys. Rev. Lett.* **85** 4024
[4] Nicole C, Offerhaus H L, Vrakking M J J, Lépine F and Bordas C 2002 *Phys. Rev. Lett.* **88** 133001
Bordas C, Lépine F, Nicole C, and Vrakking M J J 2003 *Phys. Rev.* A **68** 012709
Lépine F, Bordas C, Nicole C, and Vrakking M J J 2004 *Phys. Rev.* A **70** 033417
[5] Kondratovich V D and Ostrovsky V N 1990 *J. Phys. B: At. Mol. Opt. Phys.* **23** 3785
Cohen S, Harb M M, Ollagnier A, Robicheaux F, Vrakking M J J, Barillot T, Lépine F and Bordas C 2013 *Phys. Rev. Lett.* **110** 183001
Stodolna AS, Rouzée A, Lépine F, Cohen S, Robicheaux F, Gijsbertsen A, Jungmann J H, Bordas C and Vrakking M J J 2013 *Phys. Rev. Lett.* **110** 213001
Stodolna AS, Lépine F, Bergeman T, Robicheaux F, Gijsbertsen A, Jungmann JH, Bordas C and Vrakking MJJ 2014 *Phys. Rev. Lett.* **113** 103002
Zhao LB, Xiao DH and Fabrikant II 2015 *Phys. Rev.* A **91** 043405
[6] Cohen S, Harb M M, Ollagnier A, Robicheaux F, Vrakking M J J, Barillot T, Lépine F and Bordas C 2016 *Phys. Rev.* A **94** 13414
[7] Stodolna A S, Lépine F, Rouzée A, Cohen S, Gijsbertsen A, Jungmann-Smith J H, Bordas C and Vrakking M J J 2017 *J. Phys. B: At. Mol. Opt. Phys.* **50** 164001
[8] Ohgoda S, Tolstikhin O I and Morishita T 2017 *Phys. Rev.* A **95** 043417
[9] Kalaitzis P, Danakas S, Lépine F, Bordas C and Cohen S 2018 *Phys. Rev.* A **97** 053412
[10] Kalaitzis P, Danakas S, Bordas C and Cohen S 2023 *Phys. Rev.* A **108** 013106
[11] Kalaitzis P, Danakas S, Ferentinou K, Lépine F, Bordas C and Cohen S 2020 *Phys. Rev.* A **102** 033101
[12] Yang H-F and Tan Y-G 2019 *J. Phys. B: At. Mol. Opt. Phys.* **52** 075008
[13] Ford K W and Wheeler J A 1959 *Ann. Phys.***7** 259
re-issued in 2000 *Ann. Phys.* **281** 608
Nussenzveig H M 1992 *Diffraction Effects in Semiclassical Scattering* (Cambridge University Press)
Adam J A 2002 *Phys. Rep.* **356** 229
[14] Cohen S, Kalaitzis P, Danakas S, Lépine F and Bordas C 2017 *J. Phys. B: At. Mol. Opt. Phys.* **50** 065002
[15] Barillot T *et al* 2017 *J. Chem. Phys.* **147** 013929
[16] Press W H, Flannery B P, Teukolsky S A, and Vetterling W T 1992 *Numerical Recipes in C: The Art of Scientific Computing* (Cambridge University Press)
Cormen T H, Leiserson C E, Rivest R L, and Stein C 2001 *Introduction to Algorithms* 2nd edn (MIT Press and McGraw-Hill) p 30
[17] Crawford F S 1989 *Am. J. Phys.* **57** 621
Makowski A J and Górska K J 2002 *Phys. Rev.* A **66** 062103
[18] Fano U 1981 *Phys. Rev.* A **24** 619
[19] Harmin D A 1981. *Phys. Rev.* A **24** 2491
Harmin D A 1982 *Phys. Rev.* A **26** 2656
Harmin D A 1984 *Phys. Rev.* A **30** 2413
[20] Giannakeas P, Robicheaux F and Greene C H 2015 *Phys. Rev.* A **91** 043424
Giannakeas P, Greene C H and Robicheaux F 2016 *Phys. Rev.* A **94** 013419
[21] Ushakov V G, Osherov V I and Medvedev E S 2019 *J. Phys.* A **52** 385302
[22] Kalaitzis P, Danakas S, Ferentinou K, Cohen S and Bordas C submitted for publication
[23] Damburg R J and Kolosov V V 1976 *J. Phys. B: At. Mol. Opt. Phys.* **9** 3149
[24] Gallagher T F 1994 *Rydberg Atoms* (Cambridge University press)
[25] NIST Atomic Spectra Database Levels Form (Available at: https://physics.nist.gov/PhysRefData/ASD/levels_form.html)
[26] Kalaitzis P, Danakas S, Bordas C and Cohen S 2019 *Phys. Rev.* A **99** 023428
[27] Eppink A T J B and Parker D H 1997 *Rev. Sci. Instrum.* **68** 3477
[28] Offerhaus H L, Nicole C, Lépine F, Bordas C, Rosca-Pruna F and Vrakking M J J 2001 *Rev. Sci. Instrum.* **72** 3245
[29] Harb M M, Cohen S, Papalazarou E, Lépine F and Bordas C 2010 *Rev. Sci. Instrum.* **81** 125111
[30] Vaillant C L, Jones M P A and Potvliege R M 2014 *J. Phys. B: At. Mol. Opt. Phys.* **47** 155001 and references there in
Vaillant C L, Jones M P A and Potvliege R M 2014 *J. Phys. B: At. Mol. Opt. Phys.* **47** 199601 (erratum)
[31] Van Regemorter H, Dy H B and Prud'homme M 1979 *J. Phys. B: At. Mol. Opt. Phys.* **12** 1053
[32] Fano U 1985 *Phys. Rev.* A **32** 617
[33] Lo J I, Chu C C, Fung H S, Lee Y Y and Yih T S 2013 *Chin. J. Phys.* **51** 56
[34] Blackman R B and Tukey J W 1958 *The Measurement of Power Spectra* (Dover Publications)
[35] Sakimoto K 1986 *J. Phys. B: At. Mol. Opt. Phys.* **19** 3011
[36] Grütter M, Zehnder O, Softley T P and Merkt F 2008 *J. Phys. B: At. Mol. Opt. Phys.* **41** 115001
[37] Robicheaux F, Wesdorp C and Noordam L D 1999 *Phys. Rev.* A **60** 1420